http://ansinet.com/itj

ITJ

ISSN 1812-5638

INFORMATION TECHNOLOGY JOURNAL

ANSInet
Asian Network for Scientific Information
308 Lasani Town, Sargodha Road, Faisalabad - Pakistan

Information Technology Journal 6 (3): 405-413, 2007
ISSN 1812-5638

Robustness in Efficient Chromosome Image Segmentation Using Discrete Cosine Transform Based Gradient Vector Flow Active Contours

[1]A. Prabhu Britto and [2]G. Ravindran
[1]Center for Medical Electronics, Department of Electronics and Communication Engineering,
[2]Faculty of Information and Communication Engineering, Anna University, Chennai 600025, India

Abstract: This research analyses Discrete Cosine Transform based Gradient Vector Flow Active Contours, a segmentation tool for chromosome spread images, which have hitherto been established as an efficient segmentation tool. Extensive research has been performed on Discrete Cosine Transform based Gradient Vector Flow Active Contours for segmentation of chromosome spread images. This study is an extended analysis in the same area. This study is expected to yield more insight on efficient segmentation of chromosome spread images using Discrete Cosine Transform based Gradient Vector Flow Active Contours.

Key words: Gradient vector flow, active contours, chromosome, segmentation

INTRODUCTION

Active contours are used extensively in computer vision and image processing applications, particularly to locate object boundaries. The main advantage of Active Contours is the ability to generate closed parametric curves from images. Problems associated with initialization and poor convergence to concave boundaries, however, have limited their utility. To overcome these difficulties in initialization and poor convergence to object boundaries, a new external force model was suggested that used a convex combination of the usual external force and a new force derived from an estimate of the local curvature of the object boundary. This force simultaneously pulled the snake toward the boundary and into the concave region (Prince and Xu, 1996b). This was later improved by Xu and Prince (1998) to form the Gradient Vector Flow (GVF) field. The resulting formulation produces external force fields that had both irrotational and solenoidal components (Xu and Prince, 1998), which had a large capture range overcoming the difficulty associated with initialization of Active Contours and it was also able to provide good convergence to concave boundaries. Tang and Acton (2004) have given an improved form of the GVF field, called the Discrete Cosine Transform (DCT) based GVF. The authors have performed extensive experimentation and analysis on the chromosome spread image segmentation performance of DCT based GVF Active Contours (Britto and Ravindran, 2005a,b, 2006a-d). In this study, the authors analyze the segmentation obtained using Discrete Cosine Transform based Gradient Vector Flow Active Contours in chromosome spread images, which have hitherto been established as an efficient segmentation tool for chromosome spread images.

ACTIVE CONTOUR MODELS

Active Contours also called as Snakes or Deformable Curves, first proposed by Kass *et al.* (1987) are energy minimizing contours that apply information about the boundaries as part of an optimization procedure. They are generally initialized by automatic or manual process around the object of interest. The contour then deforms itself iteratively from its initial position in conformity with the nearest dominant edge feature, by minimizing the energy composed of the Internal and External forces, converging to the boundary of the object of interest. The Internal forces computed from within the Active Contour enforce smoothness of the curve and External forces that are derived from the image help to drive the curve toward the desired features of interest during the course of the iterative process.

The energy minimization process can be viewed as a dynamic problem where the active contour model is governed by the laws of elasticity and lagrangian dynamics (Rueckert, 1997) and the model evolves until equilibrium of all forces is reached, which is equivalent to a minimum of the energy function. The energy function is thus minimized, making the model active.

Corresponding Author: A. Prabhu Britto, Center for Medical Electronics,
Department of Electronics and Communication Engineering,
Anna University, Chennai 600025, India

FORMULATION OF ACTIVE CONTOUR MODELS

An Active Contour Model can be represented by a curve c, as a function of its arc length τ,

$$c(\tau) = \begin{pmatrix} x(\tau) \\ y(\tau) \end{pmatrix} \quad (1)$$

with $\tau = [0...1]$. To define a closed curve, c(0) is set to equal c(1). A discrete model can be expressed as an ordered set of n vertices as $v_i = (x_i, y_i)^T$ with $v = (v_1, \ldots, v_n)$. The large number of vertices required to achieve any predetermined accuracy could lead to high computational complexity and numerical instability (Rueckert, 1997).

Mathematically, an active contour model can be defined in discrete form as a curve $x(s) = [x(s), y(s)], s\varepsilon[0,1]$ that moves through the spatial domain of an image to minimize the energy functional

$$E = \int_0^1 \frac{1}{2}(\alpha |x'(s)|^2 + \beta |x''(s)|^2) + E_{ext}(x(s))ds \quad (2)$$

where α and β are weighting parameters that control the active contour's tension and rigidity respectively (Xu and Prince, 1997). The first order derivative discourages stretching while the second order derivative discourages bending. The weighting parameters of tension and rigidity govern the effect of the derivatives on the snake.

The external energy function E_{ext} is derived from the image so that it takes on smaller values at the features of interest such as boundaries and guides the active contour towards the boundaries. The external energy is defined by

$$E_{ext} = \kappa |G_\sigma(x, y) * I(x, y)| \quad (3)$$

where, $G_\sigma(x,y)$ is a two-dimensional Gaussian function with standard deviation σ, I(x,y) represents the image and κ is the external force weight. This external energy is specified for a line drawing (black on white) and positive κ is used. A motivation for applying some Gaussian filtering to the underlying image is to reduce noise. An active contour that minimizes E must satisfy the Euler Equation

$$\alpha x''(s) - \beta x''''(s) - \nabla E_{ext} = 0 \quad (4)$$

where $F_{int} = \alpha x''(s) - \beta x''''(x)$ and $F_{ext} = -\nabla E_{ext}$ comprise the components of a force balance equation such that

$$F_{int} + F_{ext} = 0 \quad (5)$$

The internal force F_{int} discourages stretching and bending while the external potential force F_{ext} drives the active contour towards the desired image boundary. Equation 4 is solved by making the active contour dynamic by treating x as a function of time t as well as s. Then the partial derivative of x with respect to t is then set equal to the left hand side of Eq.(4) as follows

$$x_t(s,t) = \alpha x''(s,t) - \beta x''''(s,t) - \nabla E_{ext} \quad (6)$$

A solution to Eq. (6) can be obtained by discretizing the equation and solving the discrete system iteratively (Kass *et al*., 1987). When the solution x(s,t) stabilizes, the term $x_t(s,t)$ vanishes and a solution of Eq. (4) is achieved.

Traditional active contour models suffer from a few drawbacks. Boundary concavities leave the contour split across the boundary. Capture range is also limited. Hence a new external force was developed (Prince and Xu, 1996). Three guiding principles led to the development of the new external force. The first aim was the ability to add the new force to the existing force. Since the existing force was the gradient of a scalar function (the energy E_{ext}), it was an irrotational (curl-free field). According to the Helmholtz theorem, the other fundamental field component was a solenoidal (divergence-free) field. Therefore, the new field was chosen to be solenoidal. The second aim was that the new field should not disturb the equilibrium contours of the external energy in the absence of internal forces. Therefore, the new field should be zero whenever the field $-\nabla E_{ext}$ is zero. The third aim wanted the field to point toward the apex of concave boundary regions, a feature defined by the object boundary curvature. Therefore, the new field was made to use a measure of boundary curvature in its definition (Prince and Xu, 1997). This was later improved by Xu and Prince to form the Gradient Vector Flow (GVF) field. Xu and Prince (1997) presented a new external force, called Gradient Vector Flow (GVF), which was computed as a diffusion of the gradient vectors of a gray-level or binary edge map derived from the image. The resultant field had a large capture range and forces the active contours into concave regions (Xu and Prince, 1998, 2000).

The overall approach was to define a new non-irrotational external force field, called as the GVF field. The earlier idea of constructing a separate solenoidal field from an image and adding it to a standard irrotational field was improved and a more natural approach was designed in which the external force field is designed to have the desired properties of both large capture range and presence of forces that point into boundary concavities. The resulting formulation produces external force fields that had both irrotational and solenoidal components (Xu and Prince, 1998).

GRADIENT VECTOR FLOW (GVF) ACTIVE CONTOURS

Gradient Vector Flow (GVF) Active Contours use Gradient Vector Flow fields obtained by solving a vector diffusion equation that diffuses the gradient vectors of a gray-level edge map computed from the image. The GVF active contour model cannot be written as the negative gradient of a potential function. Hence it is directly specified from a dynamic force equation, instead of the standard energy minimization network. The external forces arising out of GVF fields are non-conservative forces as they cannot be written as gradients of scalar potential functions. The usage of non-conservative forces as external forces show improved performance of Gradient Vector Flow field Active Contours compared to traditional energy minimizing active contours (Xu and Prince, 1998, 2000).

The GVF field points towards the object boundary when very near to the boundary, but varies smoothly over homogeneous image regions extending to the image border. Hence the GVF field can capture an active contour from long range from either side of the object boundary and can force it into the object boundary. The GVF active contour model thus has a large capture range and is insensitive to the initialization of the contour. Hence the contour initialization is flexible.

The gradient vectors are normal to the boundary surface but by combining Laplacian and Gradient the result is not the normal vectors to the boundary surface. As a result of this, the GVF field yields vectors that point into boundary concavities so that the active contour is driven through the concavities. Information regarding whether the initial contour should expand or contract need not be given to the GVF active contour model. The GVF is very useful when there are boundary gaps, because it preserves the perceptual edge property of active contours (Kass *et al.* 1987; Xu and Prince, 1998). The GVF field is defined as the equilibrium solution to the following vector diffusion equation (Xu and Prince, 2000),

$$u_t = g(|\nabla f|)\nabla^2 u - h(|\nabla f|)(u - \nabla f) \tag{7a}$$

$$u(x,0) = \nabla f(x) \tag{7b}$$

where, u_t denotes the partial derivative of u(x,t) with respect to t, ∇^2 is the Laplacian operator (applied to each spatial component of u separately) and f is an edge map that has a higher value at the desired object boundary. The functions in g and h control the amount of diffusion in GVF. In Eq. (7), $g(|\nabla f|)\nabla^2 u$ produces a smoothly varying vector field and hence called as the smoothing term, while $h(|\nabla f|)(u-\nabla f)$ encourages the vector field u to be close to ∇f computed from the image data and hence called as the data term. The weighting functions $g(\cdot)$ and $h(\cdot)$ apply to the smoothing and data terms, respectively and they are chosen[15] as $g(|\nabla f|) = u$ and $h(|\nabla f|) = |\nabla f|^2$. $g(\cdot)$ is constant here and smoothing occurs everywhere, while $h(\cdot)$ grows larger near strong edges and dominates at boundaries. Hence, the Gradient Vector Flow field is defined as the vector field v(x, y) = [u(x, y), v(x, y)] that minimizes the energy functional

$$\varepsilon = \iint \mu(u_x^2 + u_y^2 + v_x^2 + v_y^2) + |\nabla f|^2 \, dxd \tag{8}$$

The effect of this variational formulation is that the result is made smooth when there is no data.

When the gradient of the edge map is large, it keeps the external field nearly equal to the gradient, but keeps field to be slowly varying in homogeneous regions where the gradient of the edge map is small, i.e., the gradient of an edge map ∇f has vectors point toward the edges, which are normal to the edges at the edges and have magnitudes only in the immediate vicinity of the edges and in homogeneous regions ∇f is nearly zero. μ is a regularization parameter that governs the tradeoff between the first and the second term in the integrand in Eq. (8). The solution of Eq. (8) can be done using the Calculus of Variations and further by treating u and v as functions of time, solving them as generalized diffusion equations (Xu and Prince, 1998).

DISCRETE COSINE TRANSFORM (DCT) BASED GVF ACTIVE CONTOURS

The transform of an Image yields more insight into the properties of the image. The Discrete Cosine Transform has excellent energy compaction. Hence, the Discrete Cosine Transform promises better description of the image properties. The Discrete Cosine Transform is embedded into the GVF Active Contours. When the image property description is significantly low, this helps the contour model to give significantly better performance by utilizing the energy compaction property of the DCT.

The 2D DCT is defined as

$$C(u,v) = \alpha(u)\alpha(v)\sum_{x=0}^{N-1}\sum_{y=0}^{N-1} f(x,y)\cos\left[\frac{(2x+1)u\pi}{2N}\right] \cos\left[\frac{(2y+1)v\pi}{2N}\right] \tag{11}$$

The local contrast of the Image at the given pixel location (k,l) is given by

$$P(k,l) = \frac{\sum_{t=1}^{2(2n+1)-1} w_t E_t}{d_{00}} \quad (12)$$

where,

$$E_t = \frac{\sum_{u+v=t} |d_{u,v}|}{N} \quad (13)$$

and

$$N = \begin{cases} t+1 & t<2n+1 \\ 2(2n+1)-t & t\geq 2n+1 \end{cases} \quad (14)$$

Here, w_t denotes the weights used to select the DCT coefficients. The local contrast P(k,l) is then used to generate a DCT contrast enhanced Image (Tang and Acton, 2004), which is then subject to selective segmentation by the energy compact gradient vector flow active contour model using Eq. (8).

RESULTS AND DISCUSSION

The characterized standardized parameters (Britto and Ravindran, 2005b, 2006a) of the DCT based GVF Active Contours are used in the DCT based GVF Active Contour formulation that was used to segment the chromosome spread images obtained from the Genomic Centre for Cancer Research and Diagnosis (GCCRD).

The segmentation was successful without any preprocessing or enhancement procedures. Therefore no preprocessing or enhancement techniques was implemented on the images obtained from the GCCRD unlike the images that were obtained from other sources that required limited preprocessing and enhancement techniques to be implemented prior to segmentation using DCT based GVF Active Contours. A few graphical results are shown in Fig. 1-5.

The segmentation errors are tabulated shown in Table 1.

The statistics obtained earlier (Britto and Ravindran, 2006d) are shown in Table 2.

An analysis of Table 1 yields the following details tabulated in Table 3.

An analysis of Table 2 yields the following details tabulated in Table 4.

Fig. 1a: Sample 1

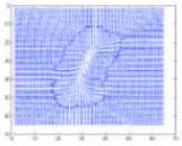

Fig. 1b: DCT GVF field

Fig. 1c: Segmented sample 1

Fig. 2a: Sample 2

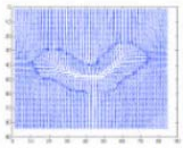

Fig. 2b: DCT GVF field

Fig. 2c: Segmented sample 2

Fig 3a: Sample 3

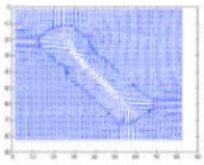

Fig. 3b: DCT GVF field

Fig. 3c: Segmented sample 3

Fig. 4a: Sample 4

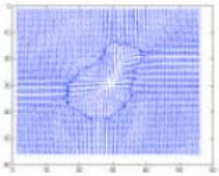

Fig. 4b: DCT GVF field

Fig. 4c: Segmented sample 4

Fig. 5a: Sample 4

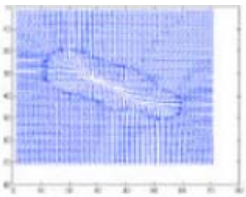

Fig. 5b: DCT GVF field

Fig. 5c: Segmented sample 5

Table 1: Segmentation error (GCCRD dataset)

Sample No.	Major axis error (Original-contour) (pixels)	Minor axis error (original-contour) (pixels)
1	-1.639411	-1.738630
2	-1.739119	-1.250510
3	-1.078454	-1.663964
4	-1.426434	-1.536739
5	-1.290367	-1.541414
6	-1.583175	-1.723457
7	-1.652096	-1.892263
8	-1.599168	-1.657190
9	-1.653724	-1.894833
10	-1.833718	-1.367811
11	-1.164023	-1.575255
12	-1.462541	-1.838559
13	-1.658229	-1.387389
14	-1.320003	-1.722582
15	-1.521426	-1.724652
16	-1.386122	-1.603411
17	-1.805429	-1.479602
18	-1.630637	-1.954916
19	-1.406267	-1.605808
20	-2.162824	-0.895561
21	-1.099298	-1.755474
22	-1.379772	-1.809109
23	-1.778165	-1.536331
24	-1.900383	-1.696603
25	-1.302674	-1.338596
26	-1.774422	-1.730759
27	-1.534535	-1.584669
28	-1.342990	-1.623543
29	-1.753152	-1.990018
30	-1.567750	-1.800871
31	-2.157066	-1.230883
32	-1.360322	-1.597205
33	-1.383456	-1.321515
34	-0.980871	-1.503225
35	-1.110669	-1.664999
36	-1.557431	-1.292485
37	-1.885984	-1.264805
38	-1.602802	-1.787419

Table 1: Continued

Sample No.	Major axis error (Original-contour) (pixels)	Minor axis error (original-contour) (pixels)
39	-1.412266	-1.540998
40	-2.245022	-0.974358
41	-1.376389	-1.531544
42	-1.207447	-1.698644
43	-1.778707	-0.794046
44	-1.485471	-1.604200
45	-1.569535	-1.565523
46	-1.442572	-1.162469
47	-2.073004	-0.875156
48	-1.705238	-1.950356
49	-1.661330	-1.345318
50	-1.074623	-1.531354
51	-1.812760	-1.483060
52	-2.069418	-1.400490
53	-1.767110	-1.268804
54	-1.205370	-1.531311
55	-1.836970	-1.280976
56	-1.575683	-1.854163
57	-1.079869	-1.563337
58	-1.202892	-1.132472
59	-2.054471	-1.481056
60	-1.261108	-1.133261
61	-1.689881	-1.559407
62	-1.992579	-1.413834
63	-1.363263	-1.805065
64	-1.742962	-1.503217
65	-1.810493	-1.799918
66	-1.329431	-1.552288
67	-1.103135	-1.693085
68	-1.402976	-1.546611
69	-1.750236	-1.905893
70	-1.394600	-1.967285
71	-1.561608	-1.496194
72	-1.422635	-1.444543
73	-2.333239	-0.472095
74	-1.183304	-1.278830
75	-1.475456	-1.609025
76	-1.369941	-1.218357

Table 1: Continued

Sample No.	Major axis error (Original-contour) (pixels)	Minor axis error (original-contour) (pixels)
77	-1.185484	-2.072397
78	-1.788363	-1.835931
79	-1.644404	-1.508064
80	-1.878734	-1.505275
81	-2.039812	-1.634831
82	-1.326524	-1.825518
83	-1.473522	-1.794276
84	-1.535446	-1.908466
85	-1.488430	-1.631116
86	-1.675665	-1.779335
87	-0.923222	-1.752778
88	-1.872654	-1.525659
89	-1.169435	-1.514405
90	-1.623659	-1.540244
91	-1.799614	-1.315558
92	-1.432972	-1.683012
93	-1.602290	-1.840383
94	-1.344840	-1.721010
95	-1.491414	-1.147922

Table 2: Segmentation error of 318 samples from 3 datasets (Britto and Ravindran, 2006d)

Sample No.	Major axis error (original-contour) (pixels)	Minor axis error (original-contour) (pixels)
1	-0.992338	-0.775864
2	-0.92236	-1.468623
3	-1.220539	-1.422845
4	-0.501174	-1.524009
5	-0.799089	-1.305647
6	-1.221461	-1.424257
7	-1.600867	-1.226584
8	-1.100319	-1.479554
9	-1.347756	-1.483728
10	-1.238815	-1.441966
11	-0.505066	-1.440641
12	-0.964582	-1.444848
13	-0.741977	-1.284649
14	-1.110216	-1.447553
15	-1.547507	-1.213763
16	-1.074563	-1.061639
17	-1.186196	-1.404811
18	-0.72746	-1.264871
19	-0.874638	-0.992366
20	-0.988652	-1.602701
21	-1.36978	-1.394782
22	-1.174377	-1.5533
23	-1.154428	-1.665724
24	-1.080455	-0.980445
25	-0.439393	-1.347199
26	-0.898015	-1.206646
27	-0.839861	-1.512812
28	-1.192257	-1.275622
29	-0.916409	-1.226661
30	-1.195272	-1.212988
31	-1.07868	-1.379909
32	-1.306899	-1.586292
33	-1.042224	-1.500224
34	-1.076928	-1.302668
35	-1.193387	-1.342275
36	-0.197003	-0.99148
37	-1.00575	-1.38379
38	-1.270241	-1.262173
39	-1.190522	-1.590911
40	-1.570681	-1.341491
41	-0.065254	-1.288282
42	-1.410574	-1.502564

Table 2: Continued

Sample No.	Major axis error (original-contour) (pixels)	Minor axis error (original-contour) (pixels)
43	-0.958566	-1.330908
44	-1.144716	-1.57406
45	-1.149548	-0.808631
46	-1.448154	-0.922816
47	-0.733335	-1.211525
48	-0.752482	-1.10831
49	-0.831605	-1.136843
50	-1.445496	-1.200295
51	-0.437316	-0.941172
52	-1.180835	-0.88306
53	-1.100511	-0.982329
54	-0.848166	-0.813109
55	-0.851951	-0.858608
56	-1.426008	-1.367665
57	-1.087917	-1.258182
58	-1.007871	-1.570674
59	-1.141832	-1.247494
60	-1.055122	-1.233528
61	-1.045525	-1.472894
62	-1.245984	-1.178031
63	-1.245907	-0.947974
64	-1.093021	-0.606021
65	-1.47522	-0.652076
66	-1.64811	-1.212763
67	-1.353749	-1.02046
68	-1.535466	-1.343574
69	-0.819889	-1.381083
70	-1.524468	-1.525374
71	-1.118025	-1.056934
72	-1.172888	-1.083572
73	-1.44782	-1.46856
74	-1.398303	-0.825764
75	-1.154896	-1.767251
76	-1.674697	-1.825242
77	-0.811548	-1.490772
78	-1.055484	-1.121062
79	-1.465084	-1.592714
80	-0.929835	-1.447415
81	-1.174461	-1.414124
82	-1.318498	-1.8509
83	-1.283027	-1.823691
84	-1.705439	-1.803142
85	-1.128187	-1.789434
86	-1.306756	-1.810684
87	-1.686564	-1.761213
88	-1.548591	-1.838386
89	-1.784505	-1.418702
90	-1.501609	-1.562417
91	-1.750446	-1.689731
92	-1.71437	-1.491664
93	-1.291892	-1.611415
94	-1.11535	-1.438064
95	-1.167061	-0.8466
96	-0.35002	-1.269065
97	-1.659774	-1.446062
98	-1.32436	-1.443249
99	-0.83952	-1.302856
100	-1.463432	-1.491251
101	-1.347055	-1.44058
102	-0.773156	-0.935695
103	-0.923166	-1.434925
104	-0.829436	-1.525105
105	-1.091322	-1.243935
106	-1.712274	-1.258548
107	-0.653843	-1.250144
108	-0.99551	-1.435568

Table 2: Continued

Sample No.	Major axis error (original-contour) (pixels)	Minor axis error (original-contour) (pixels)
109	-1.553695	-1.124056
110	-1.258162	-1.596631
111	-1.397013	-1.573557
112	-1.340142	-1.607407
113	-1.17887	-1.57955
114	-1.463692	-1.854034
115	-1.838972	-1.157378
116	-1.54852	-1.644791
117	-1.079141	-1.787633
118	-1.044313	-1.371569
119	-0.812709	-1.740844
120	-1.465677	-1.278652
121	-1.158921	-1.450319
122	-1.598489	-1.628363
123	-1.432994	-1.53496
124	-1.404522	-1.65714
125	-1.346072	-1.782505
126	-1.363875	-1.654695
127	-1.295777	-1.560376
128	-1.754922	-1.492702
129	-0.518929	-1.02551
130	-1.526409	-1.328446
131	-0.984185	-0.880658
132	-1.258347	-1.627511
133	-1.318128	-1.283184
134	-1.227557	-1.7912
135	-1.399076	-1.634108
136	-1.507578	-1.69494
137	-1.621468	-1.804087
138	-1.24531	-1.709619
139	-1.423018	-1.669788
140	-1.808238	-1.488371
141	-1.395784	-1.600006
142	-1.464432	-1.86732
143	-1.251273	-1.339695
144	-1.229269	-1.495073
145	-1.47127	-1.167317
146	-0.771764	-1.472024
147	-1.521195	-1.478963
148	-1.783761	-1.774405
149	-1.235948	-1.84757
150	-1.285183	-1.774674
151	-1.679062	-1.835052
152	-1.640928	-1.70609
153	-1.541237	-1.779609
154	-0.877035	-1.712658
155	-1.566723	-1.608762
156	-1.602352	-1.586636
157	-1.629934	-1.681697
158	-1.390202	-1.528689
159	-1.304914	-1.38873
160	-1.459184	-1.766559
161	-1.214108	-1.377772
162	-1.31448	-1.66411
163	-1.630155	-1.3727
164	-1.365475	-1.42156
165	-1.702189	-1.599185
166	-1.419314	-1.647043
167	-1.65577	-1.554056
168	-1.055188	-1.640279
169	-1.610589	-1.323203
170	-1.475299	-1.466665
171	-1.620967	-1.761993
172	-1.503408	-1.508958
173	-1.224074	-1.497617
174	-1.488749	-1.756952

Table 2: Continued

Sample No.	Major axis error (original-contour) (pixels)	Minor axis error (original-contour) (pixels)
175	-1.532382	-1.74492
176	-1.372709	-1.799141
177	-1.329297	-1.565067
178	-1.380508	-1.383839
179	-1.767232	-1.656502
180	-1.025227	-1.728641
181	-1.54005	-1.656387
182	-1.729187	-1.152385
183	-1.204434	-1.516629
184	-0.999306	-1.787821
185	-1.301427	-1.716286
186	-1.620044	-1.611656
187	-1.611729	-1.702758
188	-0.942169	-1.373288
189	-1.578107	-1.561296
190	-1.263612	-1.434885
191	-1.289469	-1.483246
192	-1.55792	-1.798453
193	-1.204962	-1.267298
194	-1.459965	-1.782017
195	-1.484583	-1.771178
196	-1.058926	-1.360518
197	-1.547085	-1.753642
198	-1.485021	-1.734517
199	-1.60663	-1.437836
200	-1.404311	-1.503494
201	-1.709402	-1.801799
202	-1.627122	-1.647771
203	-1.584391	-1.525702
204	-1.522303	-1.547991
205	-1.582705	-1.745284
206	-1.431554	-1.82118
207	-1.490827	-1.577347
208	-1.675608	-1.801507
209	-1.828339	-1.348932
210	-1.681518	-1.459575
211	-1.45422	-1.509668
212	-1.665636	-1.570325
213	-1.752641	-1.513405
214	-1.358698	-1.449
215	-1.487115	-1.635433
216	-1.686671	-1.273019
217	-1.752856	-1.649362
218	-1.900074	-1.68043
219	-1.752448	-1.643347
220	-1.152526	-1.67732
221	-1.710575	-1.5484
222	-1.773404	-1.376732
223	-1.689524	-1.390253
224	-1.276341	-1.647427
225	-1.366881	-1.710289
226	-1.265684	-1.457832
227	-1.680785	-1.641979
228	-1.60843	-1.436173
229	-1.010978	-1.240965
230	-1.179091	-1.59647
231	-1.149023	-1.59096
232	-1.737113	-1.165559
233	-1.356088	-1.59542
234	-1.807089	-1.370582
235	-1.462768	-1.063663
236	-1.034233	-1.68603
237	-1.433536	-1.109771
238	-1.6823	-1.373301
239	-1.029103	-1.614541
240	-1.236116	-1.603621

Table 2: Continued

Sample No.	Major axis error (original-contour) (pixels)	Minor axis error (original-contour) (pixels)
241	-1.063092	-1.417443
242	-1.383465	-1.330554
243	-1.963482	-1.273824
244	-1.327874	-0.997859
245	-1.158409	-1.130184
246	-1.156317	-0.792302
247	-0.62158	-0.98635
248	0.095851	-1.088073
249	-1.324107	-1.108896
250	-1.420628	-0.690222
251	-1.022918	-1.515858
252	-0.535967	-1.084688
253	-0.93526	-1.358631
254	-1.129792	-1.32887
255	-1.320984	-1.396253
256	-1.591811	-1.627622
257	-1.088018	-1.671276
258	-1.357965	-1.760885
259	-1.577488	-0.876602
260	-1.476353	-1.662791
261	-1.642213	-1.604517
262	-1.725341	-1.644339
263	-1.30636	-1.267891
264	-1.444416	-1.348944
265	-1.724593	-1.450149
266	-1.330143	-1.284747
267	-1.221269	-1.496198
268	-1.443207	-1.49924
269	-0.442626	-0.885055
270	-1.511963	-1.26339
271	-0.555771	-1.341032
272	-1.128759	-1.370847
273	-0.459103	-1.022623
274	-1.794951	-0.474824
275	-0.759098	-0.927194
276	-0.808342	-1.103186
277	-0.676985	-0.421066
278	-1.565786	-1.648637
279	-0.7794	-1.120196
280	-0.882272	-1.845699
281	-0.608516	-0.766655
282	-1.094076	-0.863614
283	-0.055934	-1.076586
284	-1.341164	-0.547116
285	-0.761	-1.101531
286	-0.512211	-1.347769
287	-1.042111	-1.063376
288	-1.288005	-1.418914
289	-0.909784	-1.265791
290	-1.095826	-1.361934
291	-1.584977	-1.202296
292	-0.686175	-1.061453
293	-0.525987	-1.036333
294	-1.25896	-0.55402
295	-1.076612	-1.43257
296	-0.886056	-1.548886
297	-1.696229	-1.073518
298	-1.018286	-1.067022
299	-0.544296	-1.06371
300	-1.04393	-0.786409
301	-1.286283	-1.440459
302	-1.106099	-1.314023
303	-1.341717	-1.610172
304	-1.367762	-1.356322
305	-1.409923	-1.678939
306	-1.195844	-1.458923

Table 2: Continued

Sample No.	Major axis error (original-contour) (pixels)	Minor axis error (original-contour) (pixels)
307	-1.567084	-1.466317
308	-0.994639	-1.134234
309	-0.75426	-1.147051
310	-1.050517	-1.333934
311	-1.639236	-1.128819
312	-0.676687	-1.228812
313	-0.955413	-1.279929
314	-1.537955	-1.118126
315	-0.850002	-1.231304
316	-1.567386	-1.680767
317	-0.924677	-1.443811
318	-0.838291	-1.152576

Table 3: Error analysis of Table 1

	Major Axis		Minor Axis	
Samples	Max Abs Error (pixels)	Min Abs Error (pixels)	Max Abs Error (pixels)	Minor Abs Error (pixels)
Range of error values (Genomic center 95 samples)	2.333239	0.923222	2.072397	0.472095
Mean error for Genomic Center (95 samples)	1.553730		1.548292	

Table 4: Error analysis of Table 2

	Major Axis		Minor Axis	
Samples	Max Abs Error (pixels)	Min Abs Error (pixels)	Max Abs Error (pixels)	Minor Abs Error (pixels)
NCI NIH (218 samples)	1.900074	0.065254	1.867320	0.606021
Detcheva (50 samples)	1.963482	0.095851	1.760885	0.690222
Wisc (50 samples)	1.794951	0.055934	1.845699	0.421066
Range of Error values (318 samples)	1.963482	0.055934	1.867320	0.421066
Mean error for NCI NIH (218 samples)	1.282728		1.451902	
Mean error for Detcheva (50 samples)	1.335659		1.384717	
Mean error for WISC samples	1.029179		1.185355	
Mean error for 318 samples	1.251185		1.399428	

Comparison of Table 3 and 4 indicates that the new results have a slightly higher error values which can be acceptable taking into account the 1 pixel wide contour thickness and the 1 pixel contour iteration step size.

Table 3 and 4 convey more significant information. From Table 4, we find that the mean errors along the major and minor axes differ very significantly, whether the datasets were taken individually or collectively together as three datasets. But Table 3 conveys that the mean error along the major and minor axis is very close to each other.

When the mean error along the major axis and the minor axis are close to each other and also slightly higher, it implies that there is scope for more improvement in segmentation results. Recalling from earlier paragraphs in this paper, we realize that no preprocessing and no enhancement have been applied to the chromosome spread images prior to segmentation using DCT based GVF Active Contours.

Summarizing the findings, no preprocessing and no enhancement has been applied to the chromosome spread images prior to segmentation using DCT based GVF Active Contours. Still, the segmentation scheme using standardized parameters for DCT based GVF Active Contours was able to give good segmentation results on chromosome spread images obtained from the GCCRD, accompanied with scope for improvement. These inferences point very much towards the direction of robustness for the already established efficient DCT based GVF Active Contours for chromosome spread image segmentation.

ACKNOWLEDGMENT

The authors express their thanks to Dr. Michael Difilippantonio (Staff Scientist at the Section of Cancer Genomics, Genetics Branch/CCR/NCI/NIH, Bethesda MD); Prof. Ekaterina Detcheva (Artificial Intelligence Department, Institute of Mathematics and Informatics, Sofia, Bulgaria); Prof. Ken Castleman and Prof. Qiang Wu (Advanced Digital Imaging Research, Texas); Wisconsin State Laboratory of Hygiene (http://worms.zoology.wisc.edu/zooweb/Phelps/karyotype.html) and the Genomic Centre for Cancer Research and Diagnosis (GCCRD) (http://www.umanitoba.ca/institutes/manitoba_institute_cell_biology/GCCRD/GCCRD_Homepage.htm) for providing chromosome spread images.

REFERENCES

Britto, A.P. and G. Ravindran, 2005a. A review of deformable curves from the perspective of chromosome image segmentation. J. Med. Sci., 5: 363-370

Britto, A.P. and G. Ravindran, 2005b. Comparison of boundary mapping efficiency of gradient vector flow active contours and their variants on chromosome Spread images. J. Applied Sci., 5: 1452-1460

Britto, A.P. and G. Ravindran, 2006a. Boundary mapping of chromosome spread images using optimal set of parameter values in discrete cosine transform based gradient vector flow active contours. J. Applied Sci., 6: 1351-1361

Britto, A.P. and G. Ravindran, 2006b. Detection of specific human chromosomal abnormalities using discrete cosine transform based gradient vector flow active contours. Biotechnology, 5: 111-117.

Britto, A.P. and G. Ravindran, 2006c. Evaluation of standardization of curve evolution based boundary mapping technique for chromosome spread images. Inform. Technol. J., 5: 94-107.

Britto, A.P. and G. Ravindran, 2006d. Segmentation of chromosome spread images using discrete cosine transform based gradient vector flow active contours-an analysis. J. Med. Sci., 6: 117-124

Kass, M., A. Witkin and D. Terzopoulos, 1987. Snakes: active contour models. Intl. J. Comp. Vision 1. pp: 321-331

Prince, J.L. and C. Xu, 1996. A new external force model for snakes. Image and Multidimensional Signal Processing Workshop, pp: 30-31

Rueckert, D., 1997. Segmentation and tracking in cardiovascular MR images using geometrically deformable models and templates. Ph.D Thesis, Imperial College of Science, Technology and Medicine, London

Tang, J. and S.T. Acton, 2004. A DCT based gradient vector flow snake for object boundary detection, Image Analysis and Interpretation, 2004. 6th IEEE Southwest Symposium, pp: 157-161

Xu, C. and J.L. Prince, 1997. Gradient Vector Flow: A New External Force for Snakes, IEEE Proc. Conf. Comp. Vis. Patt. Recog. (CVPR'97), pp: 66-71.

Xu, C. and J.L. Prince, 1998. Snakes, shapes and gradient vector flow, IEEE Trans. Image Processing, 7: 359-369

Xu, C. and J.L. Prince, 2000. Gradient Vector Flow Deformable Models, In: Handbook of Medical Imaging, Academic Press, pp: 159-170.